Journal of
Synchrotron
Radiation

ISSN 0909-0495

Received 26 November 2008
Accepted 20 January 2009

A new ultra-high-vacuum variable temperature and high-magnetic-field X-ray magnetic circular dichroism facility at LNLS

J. J. S. Figueiredo,[a,b] R. Basilio,[b] R. Landers,[a,b] F. Garcia[b] and A. de Siervo[a,b]*

[a]Departamento de Física Aplicada, Instituto de Física 'Gleb Wataghin', Universidade Estadual de Campinas, 13083-970 Campinas, SP, Brazil, and [b]Laboratório Nacional de Luz Síncrotron, 13083-970 Campinas, SP, Brazil. E-mail: asiervo@ifi.unicamp.br

X-ray magnetic circular dichroism (XMCD) is one of the most powerful tools for investigating the magnetic properties of different types of materials that display ferromagnetic behavior. Compared with other magnetic-sensitive techniques, XMCD has the advantage of being element specific and is capable of separating the spin and magnetic moment contributions associated with each element in the sample. In samples involving, for example, buried atoms, clusters on surfaces or at interfaces, ultrathin films, nanoparticles and nanostructures, three experimental conditions must be present to perform state-of-the-art XMCD measurements: high magnetic fields, low temperatures and an ultra-high-vacuum environment. This paper describes a new apparatus that can be easily installed at different X-ray and UV beamlines at the Brazilian Synchrotron Light Laboratory (LNLS). The apparatus combines the three characteristics described above and different methods to measure the absorption signal. It also permits *in situ* sample preparation and transfer to another chamber for measurement by conventional surface science techniques such as low-energy electron diffraction (LEED), reflection high-energy electron diffraction (RHEED), X-ray photoelectron spectroscopy (XPS) and X-ray photoelectron diffraction (XPD). Examples are given of XMCD measurements performed with this set-up on different materials.

Keywords: magnetism; surface magnetism; dichroism; XMCD; nanoparticles; ultrathin films.

1. Introduction

Materials science, particularly nanoscience, has received much attention from basic and applied researchers owing to the possibilities of engineering selected and unique chemical and physical properties, conventionally related to the atomic or nanometric dimensions of such materials. These new materials have properties not found in conventional bulk phases, which opens up several possibilities for technological applications. Numerous examples can be found in the literature demonstrating unique catalytic, optical, electronic and magnetic properties found in clusters and nanoparticles (Besenbacher *et al.*, 1998; Chen & Goodman, 2006; Chang, 2007; Avouris *et al.*, 2007; Ge *et al.*, 2007). It has been clearly shown that magnetic behavior depends on the size, electronic and atomic structure of nanoparticles, clusters and ultrathin films (Lau *et al.*, 2002; Dudzik *et al.*, 1999; Rupp *et al.*, 2008). For example, Lau *et al.* (2002) demonstrated enhanced magnetic behavior and angular to spin momentum contribution dependence on the number of atoms in very small (only a few atoms) iron clusters. Similarly, Dudzik *et al.* (1999) described the dependence of the blocking temperature on Co cluster size, ranging from 300 to 12000 atoms. Another fascinating example was recently presented by P. Vargas' group, demonstrating the possibility of designing magnetic nanostructures by inducing a structural phase transition in ultrathin films of Fe/Cu(100) by using ion-beam bombardment (Rupp *et al.*, 2008); this has huge potential for applications in data-storage devices and spintronics.

Recently, a number of theoretical and experimental groups have been studying the possibility of inducing ferromagnetic behavior in non-ferromagnetic elements such as Au and Pd by modifying their electronic and/or geometric structure. It might be very useful to combine noble metal properties with magnetism for a number of applications. Several theoretical studies (Scherz *et al.*, 2002; Hüger & Osuch, 2003; Delin *et al.*, 2004; Alexandre *et al.*, 2006) claim that it is possible to produce ferromagnetic palladium just by changing the stacking of the Pd layers from f.c.c. to h.c.p. or by expanding their lattice parameter. From an experimental point of view, to demonstrate and understand the physical mechanism involved in such systems certainly would contribute to the understanding of nanomagnetism, and might be important for future break-

throughs in the area. Nevertheless, the topic is still controversial and an open question, since, to the best of our knowledge, there is not an incontestable published experimental result demonstrating that the origin of the ferromagnetic signal derives from the Pd atoms in pure Pd particles, nanowires or ultrathin films and not from contaminants, or is induced by other magnetic materials or even from experimental artifacts (de Siervo *et al.*, 2007; Hüger & Osuch, 2005; Taniyama *et al.*, 1997; Abraham *et al.*, 2005). Therefore, it is essential to identify carefully the contributions to the ferromagnetic signal using an element-specific technique.

X-ray magnetic circular dichroism (XMCD) has been shown, over the last decades, to be an extremely powerful tool for the study of magnetism in materials displaying ferromagnetic coupling (Abraham *et al.*, 2005; Thole *et al.*, 1992; Wu *et al.*, 1992; Wu & Freeman, 1994; Carra *et al.*, 1993; Chen *et al.*, 1995; Vogel & Sacchi, 1996; Gambardella *et al.*, 2003). The XMCD signal can be understood, in simple terms, as the difference between the photo-absorption cross sections for a magnetized sample excited with left and right polarized light. It is possible to show that the XMCD signal can be obtained in an equivalent mode by fixing the polarization (left or right) and inverting the applied magnetic field (parallel or antiparallel to the direction of the light propagation). The XMCD signal is obtained from inner shell absorption edges through electronic transitions between core states to unoccupied valence states. In transition metals such as Fe, Ni and Co, the largest contribution to the XMCD signal involves $p \rightarrow d$ dipole transitions ($L_{2,3}$ electrons $\rightarrow$ unoccupied d valence states). In the simplest view, we can interpret the XMCD signal to be proportional to the difference in the spin-up and spin-down occupation of the unoccupied d states in the valence shell of the absorbing atoms, which acts like a spin-polarized detector. This means that XMCD is able to probe the local magnetic moment of a specific absorbing element. In some cases it is also possible to determine the magnetic behavior of different chemical states of the atoms, depending on the element and the spectral resolution of the beamline. However, it has been demonstrated that the complete theoretical description of the XMCD sum rules can be very complicated. The one-electron picture is an oversimplification, as it is necessary to take into account several aspects such as a more realistic description of the electronic and atomic structure. This is especially true for systems with low dimensionality. However, compared with other techniques, XMCD is able to provide valuable information that might lead to a better understanding of the physical mechanisms behind the magnet behavior of materials. One very remarkable result obtained by XMCD that exemplifies the power of this technique was presented by Gambardella *et al.* (2003) who studied the magnetic properties of the ultimate systems, isolated single atoms at surfaces.

As mentioned earlier, for a class of new materials such as buried atoms at interfaces, nanoparticles, clusters and ultrathin films, XMCD measurements are very appropriate for magnetic characterization, but in most cases they need to be performed under ultra-high-vacuum (UHV) conditions, with high applied magnetic fields and low sample temperature. In this paper, we describe in detail the apparatus that was built at the Brazilian Synchrotron Light Laboratory (LNLS) and present results obtained with this new set-up; we also put forward suggestions for future improvements.

2. Experimental set-up

The experimental set-up consists of a very compact UHV chamber with base pressure of about 5×10^{-10} mbar after bakeout, with the possibility of reducing the base pressure by almost one order of magnitude during measurements at low temperature (LT). All parts of the chamber are made of 316L stainless steel. The upper part of the chamber supports a manipulator, sample preparation and transfer mechanism, and the pumping system that combines a turbo-molecular and a sputter ion pump. The lower part is composed of a narrow chamber that is fixed between the pole pieces of an electromagnet. The pole pieces are separated by a gap of 26 mm, with 22 mm of internal space in the chamber at this region. The pole pieces have a central hole through which a $\frac{1}{2}$" (1.27 cm) tube joins the chamber to the beamline. The magnetic field is concentrated in the sample region using the pole pieces formed by an external structure of yoke and two cones of low-carbon iron. The geometry of the cones, including the central holes and the gap spacing, was optimized by simulations to obtain an intense and homogeneous magnetic field in the sample region. Fig. 1 shows the main parts of the XMCD set-up, and Fig. 2 presents a simulation of the magnetic field distribution and the measured magnetic field in the sample region as a function of the current in the coils. The remanent field at the sample region was 60 Oe after applying 17 kOe. We expected that it would be linear and lower than 0.4% of the maximum applied magnetic field. The temperature, water flow and electrical current in the magnets are continuously measured and interlocked to prevent overheating and to stabilize the intensity of the magnetic field. In the standard XMCD configuration, in samples with magnetic anisotropy perpendicular to the surface, for example, circularly polarized light propagates through the hole in the pole piece and impinges on the sample perpendicularly to its surface. The sample manipulator permits sample rotation to measure the XMCD signal in other configurations, for example in samples with magnetic anisotropy parallel to the surface.

The XMCD chamber can be easily installed in three different UHV beamlines at the LNLS: SXS (soft X-ray spectroscopy) beamline (1000–6000 eV) (Abbate *et al.*, 1999), SGM (spherical grating monochromator) beamline (250–1000 eV) (de Castro *et al.*, 2001) and TGM (toroidal grating monochromator) beamline (12–300 eV) (Fonseca & Castro, 1998). In these beamlines, light with almost 70% circular polarization is obtained by positioning the beamline slits out of the plane of the electron storage ring. In this way of producing circularly polarized light, the photon flux and degree of polarization are correlated, limiting the optimization of both. For the SGM beamline the photon flux for 65% circular polarized light at the region of the Fe, Ni and Co L

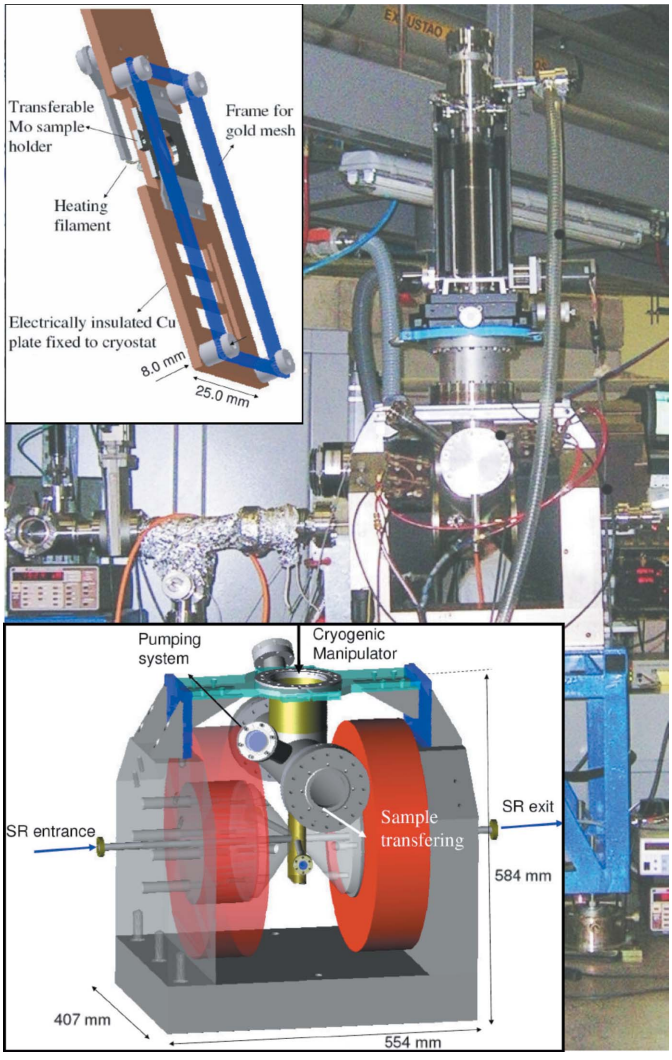

Figure 1
The UHV XMCD chamber installed at the SXS beamline. The lower inset shows a detailed CAD drawing of the main chamber. The upper inset shows the sample holder.

edges is about 1.4×10^{10} photons s^{-1} (100 mA)$^{-1}$ (0.1% bandwidth)$^{-1}$. The resolving power $E/\Delta E$ at this energy region is better than 1500. In the near future, it will be possible to use this set-up on the VUV EPU-undulator beamline (100–1000 eV) combining high-resolution spectroscopy with fully circular or linear polarized light (Reininger & Castro, 2005), which will dramatically improve the quality of the experiments. Fig. 1 shows the XMCD set-up installed at the SXS beamline.

For sample cooling, two options have been constructed. One uses simple liquid-nitrogen cooling, and with this set-up it is possible to reach 120 K at the sample. Temperature is measured using electrically insulated E-type (Cromel/Constantan) thermocouples fixed to the sample holder. As the sample holder is relatively small, it is possible to rotate the sample relative to the magnetic field. For measurements in the range ~8–450 K, a modified liquid He cryocooler from Advanced Research Systems Inc. is used, but, owing to the need for heat shielding, sample rotation is rather limited. In

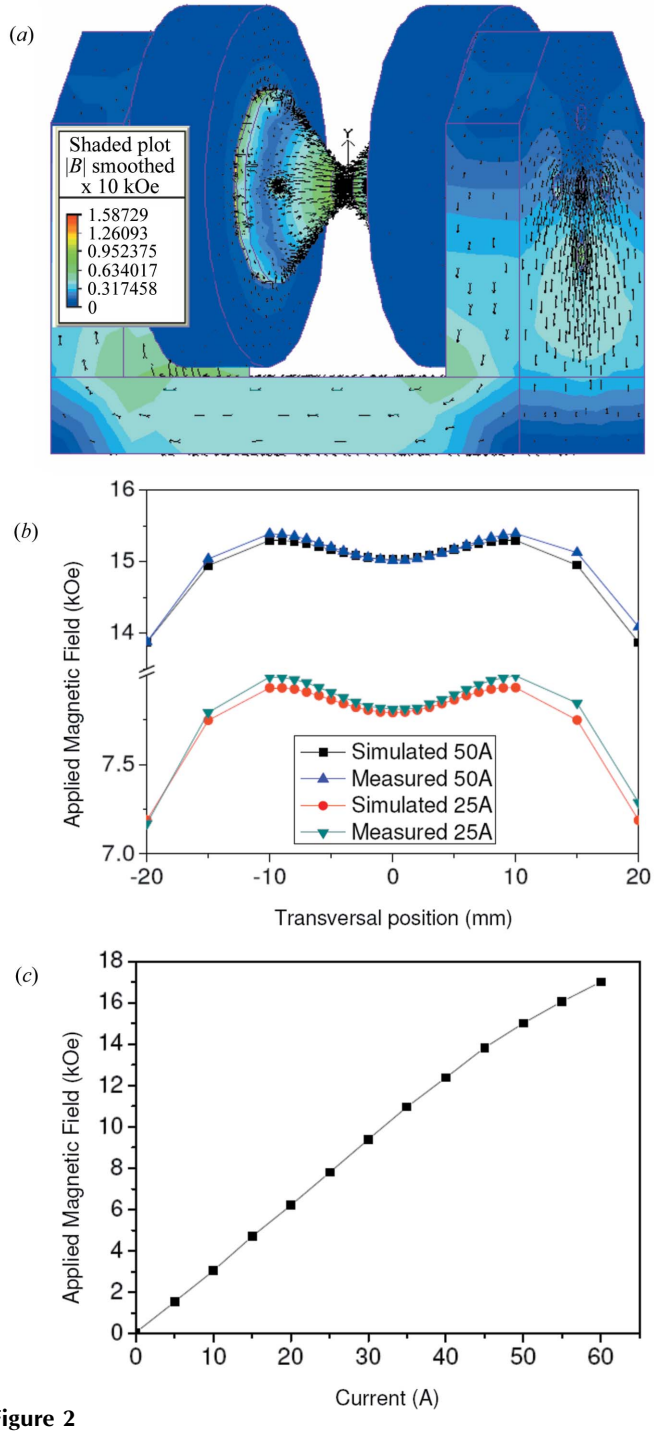

Figure 2
(*a*) A three-dimensional simulation of the magnetic field distribution and temperature in the magnetic coils for an applied current of 50 A. (*b*) Homogeneity of the magnetic field at the sample region (simulations and measurements). (*c*) Measured magnetic field as a function of the current.

this case the temperature is measured by a silicon diode, model DT-670B-SD from LakeShore Cryotronics Inc., attached to the sample holder. The sample holder (inset in Fig. 1) allows sample transfer and accommodates several samples at the same time. It also allows the absorption signal to be detected by two modes: TEY (total electron yield) or transmission through the sample. For the TEY mode, the

Table 1
Sum rules determination of the spin and orbital moment contributions for Fe and Ni ultrathin films.

The number of 3*d* holes is obtained by theoretical calculations from Eriksson *et al.* (1990) and has been used in this work and in the comparison with results from Chen *et al.* (1995) and Vogel & Sacchi (1996).

		This work		Literature	
Element	$n_{3d}^{\rm hol} = (10-n_{3d})$	$m_{\rm s}$ ($\mu_{\rm B}$)	m_L ($\mu_{\rm B}$)	$m_{\rm s}$ ($\mu_{\rm B}$)	m_L ($\mu_{\rm B}$)
Fe	3.50	1.94 ± 0.17	0.083 ± 0.007	1.98†	0.086†
Ni	1.78	0.58 ± 0.05	0.069 ± 0.007	0.58‡	0.060‡

† Chen *et al.* (1995). ‡ Vogel & Sacchi (1996).

absorption signal is detected by an electrometer limited to the pA range by signal-to-noise considerations. To prevent electrons from being reabsorbed, a 90% transmission gold mesh is placed in front of the sample which can be polarized by a few tens of volts, and this improves the signal-to-noise ratio. The gold mesh is especially important in the regime of high magnetic field. Detection in the transmission mode is especially interesting because it is naturally not affected by electron reabsorption effects or charging in insulating samples. In this case, the transmitted photons are detected by a photodiode SX100 from IRD (International Radiation Detection Inc.) with almost 100% of quantum efficiency. The signal is normalized by the TEY measured from a gold mesh positioned at the chamber's entrance in both cases. Two view-ports sited on the sample surface positioned at the center of the magnetic field are used for the fine positioning of the sample and also permit surface magnetic optical Kerr effect (SMOKE) measurements in the polar mode.

Up to now, two types of acquisition modes for XMCD have been used. The first consists of measuring complete absorption spectra with the magnetic field applied in one direction and immediately after with the field inverted. We have realised that, even after applying the normalization, a few differences between the spectra can be detected when the measurements take longer then 20 min. This effect is clearly related to the beam lifetime in the ring, slow drifts in its orbit and difficulties in precise positioning of the optical elements in the beamline. The second mode consists of measuring the XMCD spectra point by point, *i.e.* each photon energy in the spectra reversing the applied magnetic field in a short time using the sequence *ABBABAAB*, where *A* and *B* refer to the direction of the magnetic field parallel and anti-parallel to the incoming X-ray beam. The sequence is used to compensate for possible asymmetric artifacts. The time necessary to reverse completely the maximum magnetic field and stabilize it with the present electronics is about 1.5 s. This mode is time consuming owing to the dead time necessary to invert the magnetic field, but has the advantage of completely avoiding the problems of normalization. The second mode, as described here, is normally used in those cases where a long accumulation time is necessary to provide better statistics as, for example, in diluted samples.

Compared with other set-ups for performing XMCD in a UHV environment (see Fonseca *et al.*, 2007; Telling *et al.*, 2006; Aerenholz & Prestemon, 2005), our solution produces one of the highest magnetic fields available without using superconducting electromagnetic coils (Raoux, 2006; Funk & Friedrich, 2004). The possibility of producing an intense field of around 20 kOe (2 T) is one of the necessary conditions for studying materials with confined geometries (clusters, nanoparticles, nanowires and ultrathin films). Different detecting modes, fast inversion of the magnetic field and the possibility of *in situ* sample preparation and transfer are other advantages.

3. Results and discussion

3.1. XMCD from Ni and Fe $L_{2,3}$ edges

To test this set-up, we performed measurements on Fe and Ni films grown on Si(100) by DC sputtering. All films had a thickness of 20 nm and were covered by 2 nm of amorphous carbon to prevent oxidation. The film thickness was precisely calibrated using a quartz balance and an Alpha Step perfilometer. XMCD measurements were performed using the SGM beamline and TEY detection mode. The gold mesh in front of the sample was grounded, and the sample, at room temperature, was positioned at 45° with respect to the direction of the incoming photons. The light was estimated to be $65 \pm 5\%$ circularly polarized, and the base pressure was kept in the 10^{-9} mbar range in the experimental chamber. X-ray absorption spectroscopy (XAS) spectra across the $L_{2,3}$ edges of Ni and Fe were measured several times with the magnetic field of 10 kOe applied sequentially in opposite directions (I_+ and I_-). The difference in the respective spectra with I_+ and I_- results in the XMCD signal. Fig. 3 shows the XAS spectra and the respective XMCD signals for Ni and Fe. Despite the low photon flux for the polarized light [$\sim 1.4 \times 10^{10}$ photons s^{-1} $(100\ {\rm mA})^{-1}$ $(0.1\%\ {\rm bandwidth})^{-1}$], each complete XMCD experiment was carried out in approximately 10–15 min. We also performed measurements on CoPd, NiPd and FePd nanoparticles encapsulated on carbon nanotubes (NPs/CNT) (Roa *et al.*, 2009) with reasonable signal/noise ratio for the same acquisition time.

For these systems, it is well known that it is possible to apply the so-called sum rules for XMCD (Wu & Freeman, 1994). For each case in Fig. 3, the values for the integrals of the total absorption signal through the L_2 and L_3 edges expressed as *r*, as well as the values for the integrals of the XMCD signal related to each edge (*q* and *p*), are shown. These values are associated with the magnetic spin contribution $\langle L_{\rm S} \rangle$ and the orbital magnetic contribution $\langle L_z \rangle$ as described in the sum rules in Chen *et al.* (1995). In Table 1 there is a comparison of our results with values from the literature. Our determinations of both the spin and orbital magnetic moments per atom are in very good agreement with theoretical predictions and experimental measurements from the literature for Fe and Ni (Chen *et al.*, 1995; Vogel & Sacchi, 1996).

3.2. XMCD from Pd/Fe multilayers

Before measurements of the induced magnetic properties in the Pd $L_{2,3}$ edges of systems such as nanoparticles (bimetallic

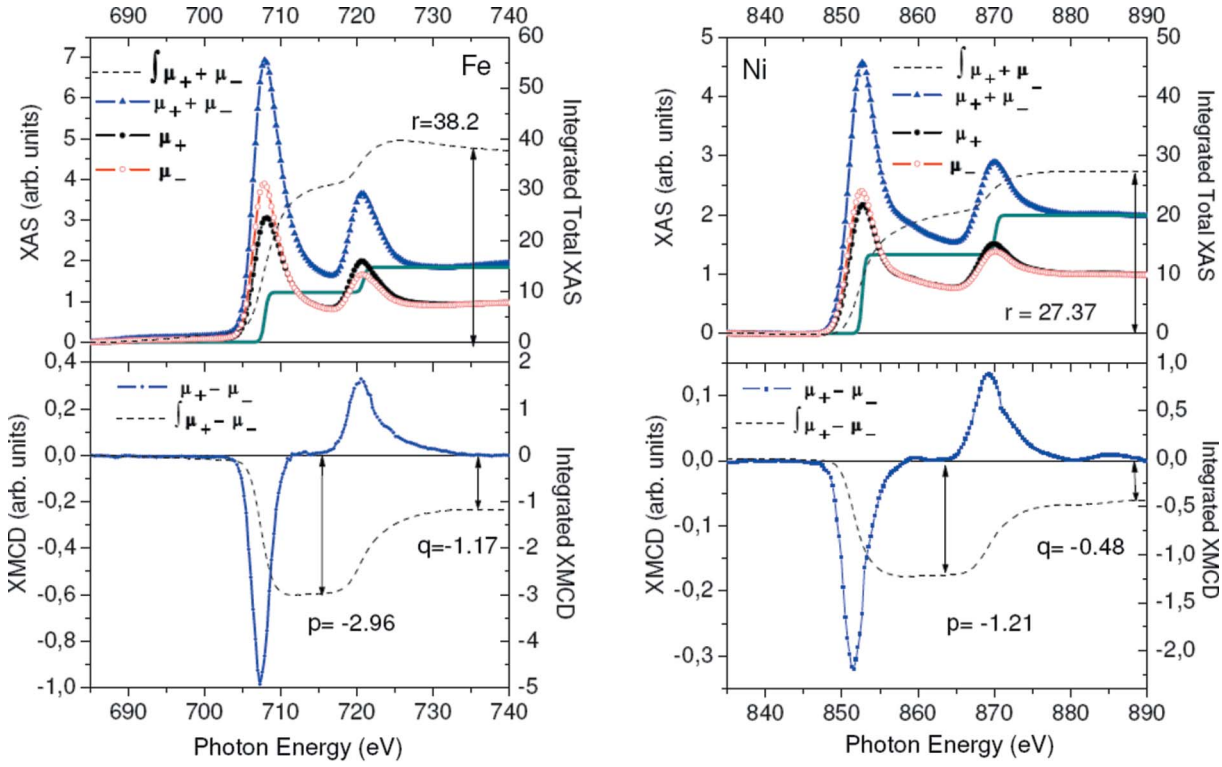

Figure 3
XMCD measurements from $L_{2,3}$ edges of Ni and Fe films on Si(100) (see text for details).

Pd NPs/CNT, Pd nanoparticles capped with thiol) and stressed Pd ultrathin films grown on graphene/SiC, for example, we tested our set-up for Pd/Fe and Pd/Co multilayers grown on Si(100). The multilayer samples were grown by DC sputtering. The result presented here is for a sample grown with 40 Å of Fe followed by 20 Å of Pd, repeated 20 times and covered with 20 Å of amorphous carbon to prevent oxidation, *i.e.* [Fe(40 Å)/Pd(20 Å)] × 20/C(20 Å).

This sample was characterized using the magnetic optical Kerr effect (MOKE), which reveals that it has an easy axis of magnetization parallel to the surface, with a saturation field of 600 Oe. For the XMCD measurements, we used the same configuration described above with fixed circularly polarized light provided by the SXS beamline. Fig. 4(*a*) shows the absorption spectra for the L_3 and L_2 edges of Pd measured with +3 kOe (I_+) and −3 kOe (I_-) of applied magnetic field. Fig. 4(*b*) shows the XMCD signal as well as its integrated curve. Applying the sum rules, we have determined the ratio between the spin and orbital magnetic contributions as being $\langle L_z\rangle/\langle L_S\rangle$ = 0.095. This value is in very good agreement with that obtained by Vogel *et al.* (1997) for a similar Pd/Fe multilayer sample. In our case, it is harder to evaluate precisely the individual values of $\langle L_z\rangle$ and $\langle L_S\rangle$ owing to beamline limitations. In contrast to the Fe and Ni edges, in Pd the large spin–orbit interaction causes the L_2 and L_3 edges to be separated by almost 160 eV. In the SXS beamline the light polarization changes from ∼40 to ∼50% at the L_3 edge and L_2 edge, respectively. For this reason the L_2 peak in the XMCD has almost the same intensity as the L_3 peak. The expected

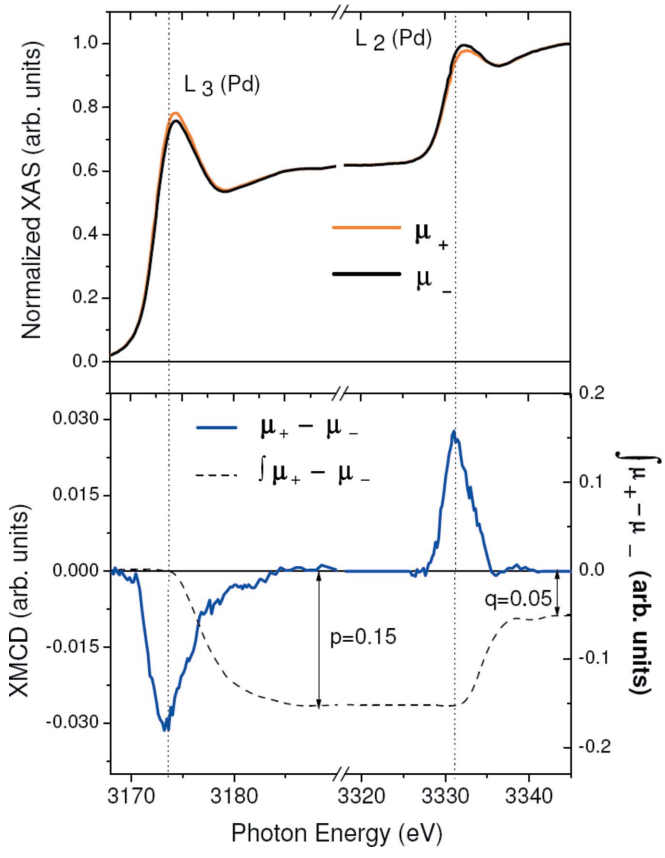

Figure 4
XMCD measurements from $L_{2,3}$ edges of Pd in Pd/Fe multilayers on Si(100) (see text for details).

value for the total magnetic contribution from Pd is in the order of 0.15 μ_B atom^{-1}. It means that $\langle L_z \rangle \simeq 0.01\ \mu_B$ atom^{-1} and $\langle L_S \rangle \simeq 0.07\ \mu_B$ atom^{-1}. These results are in very good agreement with the findings of Vogel *et al.* (1997). With this experiment we assume that our set-up is able to reach systems showing magnetic contributions in the range of $10^{-2}\ \mu_B$ atom^{-1} at least. The quality of signal/noise will depend on the photon flux and the amount of sample. In the near future, the optics of the SXS beamline will be upgraded and it is expected that this will result in an increase, by a factor of 4, in the photon flux. We believe that, with high photon flux in combination with chopping and lock-in techniques of detection of the XMCD signal, it may be possible to decrease the detectable limit in our set-up to the range of $10^{-3}\ \mu_B$ atom^{-1} at least.

4. Conclusions

This work describes a new set-up for XMCD measurements that combines a UHV environment, high magnetic field and controllable sample temperature from the cryogenic regime up to 450 K. The apparatus is versatile, permitting *in situ* sample growth or sample transfer between other chambers used to perform more conventional surface science characterizations such as LEED, XPS or XPD. It can be installed on several UHV beamlines that are suitable for measuring magnetism in different types of materials (transition metals, rare earths *etc.*). The preliminary results are consistent with the XMCD data taken from the $L_{2,3}$ edges of Fe and Ni thin films as well as from Pd $L_{2,3}$ edges of Pd/Fe and Pd/Co multilayers (not presented here). From the Pd XMCD results measured in Pd/Fe multilayers as well as on Pd/Co nanoparticles encapsulated in CNTs (results not presented here), we have evidence that our system is able to detect ferromagnetic contributions down to the range of $10^{-2}\ \mu_B$ atom^{-1}.

The authors would like to thank the LNLS staff, particularly the magnets, project and vacuum groups for their help during the construction of the XMCD UHV chamber. P. T. Fonseca and Dr F. Vicentin are acknowledged for their excellent technical support at the SGM and SXS beamlines. Furthermore, the authors would like to thank Dr A. Gobbi and M. M. Soares for their help in the preparation of the multilayer samples. JJSF would like to thank FAPESP for the studentship support. This project was supported financially by FAPESP (grant No. 2007/08244-5), CNPq and LNLS of Brazil.

References

Abbate, M., Vicentin, F. C., Compagnon-Cailhol, V., Rocha, M. C. & Tolentino, H. (1999). *J. Synchrotron Rad.* **6**, 964–972.
Abraham, D. W., Frank, M. M. & Guha, S. (2005). *Appl. Phys. Lett.* **87**, 252502.
Aerenholz, E. & Prestemon, S. O. (2005). *Rev. Sci. Instrum.* **76**, 083908.
Alexandre, S. S., Mattesini, M., Soler, J. M. & Yndurain, F. (2006). *Phys. Rev. Lett.* **96**, 079701.
Avouris, P., Chen, Z. & Perebeinos, V. (2007). *Nature Nanotechnol.* **2**, 605–615.
Besenbacher, F., Chorkendorff, I., Clausen, B. S., Hammer, B., Molenbroek, A. M., Norskov, J. & Stensgaard, I. (1998). *Science*, **279**, 1913–1915.
Carra, P., Thole, B. P., Altarelli, M. & Wang, X. (1993). *Phys. Rev. Lett.* **70**, 694–697.
Castro, A. R. B. de, Fonseca, P. T., Pacheco, J. G., da Silva, J. C. V., da Silva, E. G. L. & Santana, M. H. A. (2001). *J. Magn. Magn. Mater.* **233**, 69–73.
Chang, R. K. (2007). *Nature Photonics*, **1**, 563–564.
Chen, C. T., Idzerda, Y. U., Lin, H.-J., Smith, N. V., Meigs, G., Chaban, E., Ho, G. H., Pellegrin, E. & Sette, F. (1995). *Phys. Rev. Lett.* **75**, 152–155.
Chen, M. S. & Goodman, D. W. (2006). *Science*, **306**, 252–255.
Delin, A., Tosatti, E. & Weht, R. (2004). *Phys. Rev. Lett.* **92**, 057201.
Dudzik, E., Dürr, H. A., Dhesi, S. S., van der Laan, G., Knabben, D. & Goedkoop, J. B. (1999). *J. Phys. Condens. Matter*, **11**, 8445–8451.
Eriksson, O., Johansson, B., Albers, R. C., Boring, A. M. & Brooks, M. S. S. (1990). *Phys. Rev. B*, **42**, 2707–2710.
Fonseca, P. T. & de Castro, A. R. B. (1998). Private communication.
Fonseca, P. T., de Castro, A. R. B., Tosin, G., Citadini, J. F. & Basilio, R. (2007). *Braz. J. Phys.* **37**, 1171–1176.
Funk, T. & Friedrich, S. (2004). *Rev. Sci. Instrum.* **75**, 756–759.
Gambardella, P., Rusponi, S., Veronese, M., Dhesi, S. S., Grazioli, C., Dallmeyer, A., Cabria, I., Zeller, R., Dederichs, P. H., Kern, K., Carbone, C. & Brune, H. (2003). *Science*, **300**, 1130–1133.
Ge, J., Hu, Y. & Yin, Y. (2007). *Angew. Chem.* **46**, 7428–7431.
Hüger, E. & Osuch, K. (2003). *Europhys. Lett.* **63**, 90–99.
Hüger, E. & Osuch, K. (2005). *Phys. Rev. B*, **72**, 085432.
Lau, J. T., Föhlisch, A., Nietubyć, R., Reif, M. & Wurth, W. (2002). *Phys. Rev. Lett.* **89**, 057201.
Raoux, D. (2006). *The Synchrotron SOLEIL Newspaper*, **13**, 14–15.
Reininger, R. & Castro, A. R. B. (2005). *Nucl. Instrum. Methods Phys. Res. A*, **538**, 760–770.
Roa, D. B., Magalhães-Paniago, R., de Siervo, A., Figueiredo, J. J. S. & Lacerda, R. G. (2009). In preparation.
Rupp, W., Biedermann, A., Kamenik, B., Ritter, C., Klein, C., Platzgummer, E., Schmid, M. & Varga, P. (2008). *Appl. Phys. Lett.* **93**, 063102.
Scherz, A., Wende, H., Baberschke, K., Minár, J., Benea, D. & Ebert, H. (2002). *Phys. Rev. B*, **66**, 184401.
Siervo, A. de, de Biasi, E., Garcia, F., Landers, R., Martins, M. D. & Macedo, M. A. A. (2007). *Phys. Rev. B*, **76**, 075432.
Taniyama, T., Ohta, E. & Sato, T. (1997). *Europhys. Lett.* **38**, 195–200.
Telling, N. D., van der Laan, G., Georgieva, M. T. & Farley, N. R. S. (2006). *Rev. Sci. Instrum.* **77**, 073903.
Thole, B. T., Carra, P., Sette, F. & van der Laan, G. (1992). *Phys. Rev. Lett.* **68**, 1943–1946.
Vogel, J., Fontaine, A., Cros, V., Petroff, F., Kappler, J.-P., Krill, G., Rogalev, A. & Goulon, J. (1997). *Phys. Rev. B*, **55**, 3663–3669.
Vogel, J. & Sacchi, M. (1996). *Phys. Rev. B*, **53**, 3409–3414.
Wu, R. & Freeman, A. J. (1994). *Phys. Rev. Lett.* **73**, 1994–1997.
Wu, Y., Stöhr, J., Hermsmeier, B. D., Samant, M. G. & Weller, D. (1992). *Phys. Rev. Lett.* **69**, 2307–2310.